the contact width, and L is the nanotube length. These quantities are difficult to measure independently and calculations are model-dependent. As a guide, we apply a *JKR* model for the contact of cylinders[25] and find a contact width of 3 nm for a tube radius of 13.5 nm. Our measurements of 0.006 N m^{-1} for the friction force per unit length is then consistent with a shear stress of 2×10^6 Pa. This can be compared with a value of 5×10^6 Pa, as inferred from AFM tip/graphite measurements[16]. To compare rolling and sliding in a single tube, we can calculate the force (4 nN for $L = 590$ nm) and that would be needed to slide tube B, which in fact rolls. Finally, we note that the area under the lateral force trace is a direct measure of energy loss in rolling. For tube B, we measure an energy loss of $(8 \pm 3) \times 10^{-16}$ J per revolution. The sliding energy loss expected for this distance (85 nm) can be calculated using the frictional force of 4 nN, yielding 3×10^{-16} J.

When we compare our lateral force measurements for sliding and rolling cases, we find that the stick peaks in rolling are higher than the lateral force needed to sustain sliding, and that the energy cost for rolling is larger than that of the sliding cases. Why should the nanotubes roll? We speculate that, owing to the size and surface features of the rolling nanotubes, a stick peak for sliding in side-on pushing might exist that is larger than the threshold for rolling. Atomic-scale substrate interactions may also play a roll as we have observed this characteristic rolling only on graphite. Rolling behaviour has been accompanied by a preferential, threefold, in-plane orientation that indicates intimate nanotube/graphite contact, and perhaps lattice registry. Rolling may occur only when both the nanotube and the underlying graphite have long-range order. In these cases that there may be a barrier for sliding which is larger than that for rolling and may preclude the direct measurement of sliding friction[7]. □

Received 27 July; accepted 10 September 1998.

1. Persson, B. N. J. *Sliding Friction: Physical Properties and Applications* (Springer, Berlin, 1998).
2. Bhushan, B., Israelachvili, J. N. & Landman, U. Nanotribology: friction, wear and lubrication at the atomic scale. *Nature* **374,** 607–616 (1995).
3. Johnson, K. L. *Contact Mechanics* (Cambridge University Press, New York, 1994).
4. Mate, M. C., McClelland, G. M., Erlandsson, R. & Chiang, S. Atomic-scale friction of a tungsten tip on a graphite surface. *Phys. Rev. Lett.* **59,** 1942–1945 (1987).
5. Israelachvili, J. *Intermolecular and Surface Forces* (Academic, San Diego, 1991).
6. Binnig, G., Quate, C. F. & Gerbre, C. Atomic force microscope. *Phys. Rev. Lett.* **56,** 930–933 (1986).
7. Sheehan, P. E. & Lieber, C. M. Nanotribology and nanofabrication of MoO_3 structures by atomic force microscopy. *Science* **272,** 1158–1161 (1996).
8. Johnson, K. L. in *Micro/nanotribology and its Applications* (ed. Bhushan, B.) 157 (Kluwer Academic, Dordrecht, The Netherlands, 1997).
9. Hirano, H., Shinjo, K., Kaneko, R. & Murata, Y. Anisotropy of frictional forces in muscovite mica. *Phys. Rev. Lett.* **67,** 2642–2645 (1991).
10. Overney, R. M., Takano, H., Fujihira, M., Paulus, W. & Ringsdorf, H. Anisotropy in friction and molecular stick–slip motion. *Phys. Rev. Lett.* **72,** 3546–3549 (1994).
11. Luthi, R. *et al.* Sled-type motion on the nanometer scale: Determination of dissipation and cohesive energies of C_{60}. *Science* **266,** 1979–1981 (1994).
12. Falvo, M. R. *et al.* Bending and buckling of carbon nanotubes under large strain. *Nature* **389,** 582–584 (1997).
13. Hertel, T., Martel, R. & Avouris, P. Manipulation of individual carbon nanotubes and their interactions with surfaces. *J. Phys. Chem. B* **102,** 910–915 (1998).
14. Rapoport, L. *et al.* Hollow nanoparticles of WS2 as potential solid-state lubricants. *Nature* **387,** 791–793 (1997).
15. Bhushan, B., Gupta, B. K., Van Cleef, G. W., Capp, C. & Coe, J. V. Sublimed C^{60} films for tribology. *Appl. Phys. Lett.* **62,** 3253–3255 (1993).
16. Schwarz, U. D., Zworner, O., Koster, P. & Wiesendanger, R. Quantitative analysis of the frictional properties of solid materials at low loads. 1. Carbon compounds. *Phys. Rev. B* **56,** 6987–6996 (1997).
17. Ebbesen, T. W. & Ajayan, P. M. Large-scale synthesis of carbon nanotubes. *Nature* **358,** 220–222 (1992).
18. Taylor, R. M. *et al. SIGGRAPH '93* (ACM SIGGRAPH, New York, 1993).
19. Finch, M. *et al. ACM Symposium on Interactive 3D Graphics* (ACM SIGGRAPH, Monterey, California, 1995).
20. Prescott, J. *Mechanics of Particles and Rigid Bodies* (Longmans, Green and Co., London, 1936).
21. Baur, C. *et al.* Robotic nanomanipulation with a scanning probe microscope in a networked computing environment. *J. Vac. Sci. Tech. B* **15,** 1577–1580 (1997).
22. Mason, M. T. & Salisbury, J. K. J. *Robot Hands and the Mechanics of Manipulation* (MIT Press, Cambridge, Massachusetts, 1985).
23. Ebbesen, T. W. & Takada, T. Topological and sp^3 defect structures in nanotubes. *Carbon* **33,** 973–978 (1995).
24. Kendall, K. Rolling friction and adhesion between smooth solids. *Wear* **33,** 351–358 (1975).
25. Chaudhury, M. J., Weaver, T., Hui, C. Y. & Kramer, E. J. Adhesive contact of cylindrical lens and a flat sheet. *J. Appl. Phys.* **80,** 30–37 (1996).

Acknowledgements. We thank O. Zhou for CNT soot material, S. Paulson for helping to solve sample-preparation problems, and the entire Nanomanipulator team. The NSF, the NIH, the Office of Naval Research, and Topometrix Inc. provided financial support for this work.

Correspondence and requests for materials should be addressed to R.S. (e-mail: rsuper@physics.unc.edu).

Identifying the forces responsible for self-organization of nanostructures at crystal surfaces

K. Pohl*, M. C. Bartelt*, J. de la Figuera*, N. C. Bartelt*, J. Hrbek*† & R. Q. Hwang*

* *Sandia National Laboratories, Livermore, California 94550, USA*

The spontaneous formation of organized surface structures at nanometre scales[1,2] has the potential to augment or surpass standard materials patterning technologies. Many observations of self-organization of nanoscale clusters at surfaces have been reported[1–10], but the fundamental mechanisms underlying such behaviour—and in particular, the nature of the forces leading to and stabilizing self-organization—are not well understood. The forces between the many-atom units in these structures, with characteristic dimensions of one to tens of nanometres, must extend far beyond the range of typical interatomic interactions. One commonly accepted source of such mesoscale forces is the stress field in the substrate around each unit[1,11–13]. This, however, has not been confirmed, nor have such interactions been measured directly. Here we identify and measure the ordering forces in a nearly perfect triangular lattice of nanometre-sized vacancy islands that forms when a single monolayer of silver on the ruthenium (0001) surface is exposed to sulphur at room temperature. By using time-resolved scanning tunnelling microscopy to monitor the thermal fluctuations of the centres of mass of the vacancy islands around their final positions in the self-organized lattice, we obtain the elastic constants of the lattice and show that the weak forces responsible for its stability can be quantified. Our results are consistent with general theories of strain-mediated interactions between surface defects in strained films.

We began by depositing slightly less than one monolayer (ML) of Ag at room temperature on a clean Ru(0001) surface prepared in ultrahigh vacuum. A Ag film forms that is highly strained as a result of the ~7% lattice mismatch between Ag and Ru. A flash anneal to 750 K, to obtain an equilibrium Ag film, one single layer high, invariably produces an ordered pattern in the film (unit cell $\sim 40 \times 60$ Å) consisting of a near-square array of threading dislocations[14,15]. Subsequent exposure of this strained layer to sulphur, at room temperature, triggers strikingly complex behaviour in the Ag film, as sulphur displaces Ag atoms. Here we describe two main regimes distinguished by the sulphur coverage, θ_S.

For low $\theta_S < 0.05$ ML, scanning tunnelling microscopy (STM) images show far-separated two-dimensional vacancy islands of highly regular size, about 34 ± 11 Å diameter (Fig. 1a, b). Sulphur is found coating exposed Ru regions, including the inside of the islands where it forms ordered two-dimensional clusters (Fig. 1b inset). This is not surprising because the interaction of sulphur with Ru is considerably stronger than that with Ag, and it certainly reduces the energy cost of exposing the Ru(0001) surface by decreasing its surface energy.

The isolated vacancy islands are extremely mobile (Fig. 1a, b), significantly more so than has been reported for vacancy islands of similar size on clean metal (111) surfaces[16,17]. Islands diffuse perhaps by atoms diffusing along the edges of islands, although other mechanisms involving a flow of atoms across an island, or exchange of edge atoms with the sulphur and Ag adatom gas, could also be significant. We measured island hop rates of several hundreds of

† Permanent address: Brookhaven National Laboratory, Upton, New York 11973, USA

ångströms per minute, at room temperature, each hop averaging 50 Å between positions seemingly related to the network of dislocations in the original Ag film. This high island mobility suggests that these structures are equilibrated.

As we monitor this dilute 'gas' of islands with the STM, we often observe random formation and dissociation of small collections of islands, with island–island separations of ~50 Å (Fig. 1a, b). Strong short-range repulsions between islands seem to prevent them from coming closer to one another and coalescing. The effect of these repulsions becomes increasingly dramatic as we add more sulphur, and the density of vacancy islands, as well as the density and size of self-assembled clusters of islands, increase. Near 0.1 ML of sulphur, a stable, nearly-perfect, triangular lattice of vacancy islands forms, with island–island separations of ~53 Å, extending over each of the micrometre-wide Ru terraces (Fig. 1c). The distribution of island diameters in the lattice is also impressively narrow (±4 Å), peaked at 24 Å. Annealing to temperatures below the desorption temperature of the Ag produces no apparent changes in the lattice.

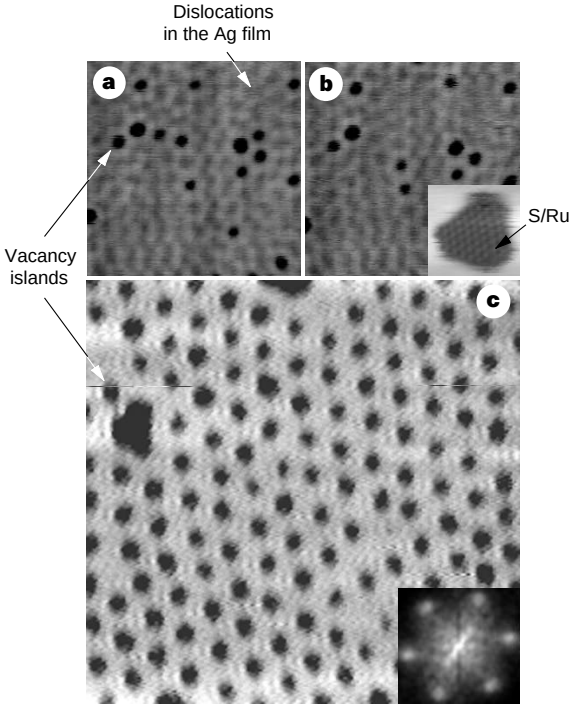

Figure 1 Low- and high-density vacancy island lattices. **a**, **b**, Two frames, 2 min apart, of an STM 'movie' of the same 480 × 480 Å area of sulphur-exposed Ag/Ru(0001). The sulphur coverage is $\theta_S \approx 0.04$ ML, and the area fraction of vacancy islands is $f \approx 0.07$. Inset in **b**, 60 × 60 Å STM image of a large vacancy island (these are immobile compared to smaller islands, but 'breathe' on the timescale of STM image acquisition.) Inside the island is a cluster of sulphur atoms. Diffusing single vacancies are often observed in such clusters, disappearing at the island edge within minutes. We note how the motion of the island edges is so rapid (compared to the rate of STM image acquisition) that they have a 'blurred' appearance. **c**, A 600 × 600 Å STM image of the vacancy island crystal (here, $\theta_S \approx 0.1$ ML and $f \approx 0.2$). Defects in the crystal include large islands (density ~2×10^{-5} Å^{-2}) and paired dislocation lines (density ~7×10^{-6} Å^{-2}). Inset in **c**, the Fourier transform of a 200 × 200 nm^2 image.

A large series of consecutive STM images reveals that the islands fluctuate about their final positions in the lattice, probably by the same mechanisms of island diffusion that were apparent in the low-island-density regime. This island motion is illustrated by the image overlay of Fig. 2a. Quantitative analysis of these fluctuations allows direct assessment of the strength of the interactions between islands, as we show next. We note that the individual island areas also fluctuate in time, perhaps via exchange of Ag edge atoms between neighbouring islands or with the adatom gas. However, we did not observe any consistent correlation between fluctuations in the island areas and those in the island positions, not even for nearest-neighbour islands. The relative amplitude of the fluctuations in the island positions is also significantly larger than that of the areas.

For analysis of the lattice fluctuations, we then followed the displacement, **u**, of the centre of mass (CM) of each island in a 450 × 450 Å array (~80 islands) with time-resolved STM, recording images of the same area at intervals of 10–20 s for nearly 4 hours. We define $\mathbf{u}(\mathbf{r}_0, t) = \mathbf{r}(t) - \mathbf{r}_0$, where $\mathbf{r}(t)$ is the position of the CM at time t of the vacancy island at the equilibrium CM position $\mathbf{r}_0$. The typical range of values for the components of **u**, obtained by marking the CM trajectories over the complete data set, is shown for one island in Fig. 2b. The motion of individual islands is correlated, reflecting interactions between neighbouring islands. Figure 2c shows clearly that **u**-values are positively correlated for neighbouring islands ('in phase' displacements being more likely, as expected for repulsive island–island interactions). This correlation decays rapidly with island–island separation.

As the measured amplitude of the island fluctuations is small, we expect them to be well described as vibrations in a harmonic crystal. (Strictly speaking, here there is no analogue of the inertia in a crystalline solid, as the motion of the islands is purely diffusive.) In this case, each component of the Fourier-transformed CM displacements is expected to fluctuate independently, while satisfying equipartion of energy. This allows a rigorous connection between the amplitude of the fluctuations and the elastic constants of the 2D island crystal[18,19]. We focus on the long-wavelength behaviour of the expectation value of the steady-state pair correlation function, defined as $G_{ij}(\mathbf{q}) = (1/A)[\hat{u}_i(\mathbf{q})\hat{u}_i(-\mathbf{q})]$, between components i and j of the Fourier-transformed displacements, $\hat{\mathbf{u}}(\mathbf{q}) = \int d^2\mathbf{r}_0 \mathbf{u}(\mathbf{r}_0) \exp(i\mathbf{q}\cdot\mathbf{r}_0)$. Here, A is the analysed area. The

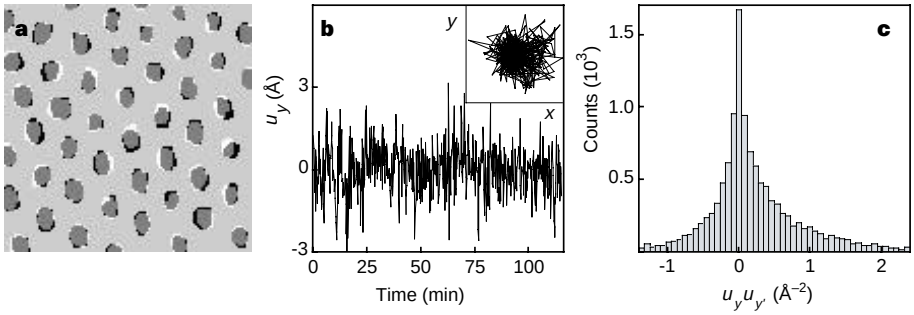

Figure 2 Thermal fluctuations in the vacancy island crystal. **a**, Overlay of two 300 × 300 Å (contrast enhanced) STM images, 20 s apart. In one of the frames the islands are black and in the other white, so the overlap is dark grey. **b**, The y-component of the CM displacement, u_y, versus time for a selected island, taken from a sequence of 690 frames, 10 s apart. The inset shows the full x–y trajectory. **c**, Distribution of the (equal-time) product $u_y u_{y'}$, of CM displacements of nearest-neighbour islands, over the 690 frames. The average is $\langle u_y u_{y'} \rangle \approx 0.26$ Å^2. Skewness, $\kappa \approx 1.8$, in this distribution reflects (positive) correlation in the motion of nearest-neighbour islands.

components i and j of $\hat{\mathbf{u}}(\mathbf{q})$ can equivalently be distinguished as components which are longitudinal (l) or transverse (t) to $\mathbf{q}$. For small, non-zero $q = |\mathbf{q}|$, equipartition of energy amongst the independent modes then gives[18,19] $G_{tt}(\mathbf{q}) = k_B T/(q^2\mu)$ and $G_{ll}(\mathbf{q}) = [k_B T/(q^2\mu)] \times [1 - (\lambda + \mu)/(\lambda + 2\mu)]$, where T is the temperature, k_B is the Boltzmann constant, and λ and μ are the elastic Lamé coefficients of the 2D lattice which govern changes in the elastic energy density. (The bulk modulus is $\lambda + \mu$; the shear modulus is μ.) Thus, estimates of λ and μ can be obtained by analysing either the slopes of G_{tt} and G_{ll} versus $1/q^2$, or the actual values of G_{tt} and G_{ll} at some (small) q.

For a 'perfectly' ordered 6×6 vacancy island cell, Fig. 3 shows that the amplitude of G_{ll} decreases rapidly with q, qualitatively as predicted. From these and similar data for G_{tt}, we measured average values of $G_{ll} \approx 3 \pm 1\,\mathrm{nm}^4$ and $G_{ll} \approx 4 \pm 2\,\mathrm{nm}^4$, for the smallest non-zero $q = 4\pi/(10\sqrt{3}b) \approx 0.14\,\mathrm{nm}^{-1}$. Thus, from the relations above, we estimate $\lambda \approx \mu \approx 0.02$–$0.04\,\mathrm{N\,m}^{-1}$. The uncertainty reflects observed variation in the values obtained at different q. These results are consistent with values obtained from the width of the gaussian distribution of mean square displacements, or from analysis of the shape and skewness of the distribution of displacement correlations for nearest-neighbour islands in Fig. 2c (K.P. *et al.*, manuscript in preparation).

In order to use the above analysis to elucidate the origin of the forces that stabilize the island vacancy lattice, one must consider two competing contributions. One is from the line tension, γ_b, which reflects the cost of creating island edges, where atoms have reduced coordination. This contribution favours the formation of a few large islands. For Ag(111), $\gamma_b \approx 0.1\,\mathrm{eV\,Å}^{-1}$ (ref. 20). To counter this tendency, there are elastic forces between the edges of neighbouring islands. These forces come from the elastic deformations of atomic positions around the edges of islands, which arise in response to the strain in the film. (Ag has a larger lattice constant than Ru, so a slight outward expansion at the island edges is expected.) The interference between these deformations leads to an interaction that is inversely proportional to the distance between pairs of island edges[12]. The proportionality constant is an energy per unit length, γ_d, which characterizes the interaction strength. The sign of this interaction depends on the cosine of the angle between pairs of edges so that neighbouring edges of adjacent islands (that are of opposite orientation) lead to a repulsive force, while edges of the same orientation from adjacent islands are attractive (weaker entropic and elastic dipole repulsions being neglected)[13]. The net contribution to the elastic energy, relative to that of a uniform film, is negative, favouring spontaneous island formation[1,11,12]. It is γ_d that we want to measure here. We note that the form of the elastic hamiltonian[11,12] assumes that the Ru substrate deforms in reaction to the elastic relaxations near the island edges: such deformation of the Ru substrate by strain in the Ag film is consistent with the results in ref. 15.

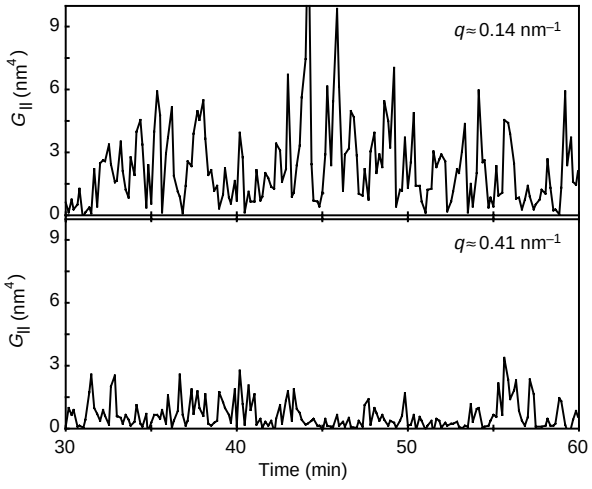

Figure 3 Analysis of correlations in the thermal displacements of neighbouring islands. The time dependence of the longitudinal pair correlation function $G_{ll}(q)$ is shown for $q \approx 0.14\,\mathrm{nm}^{-1}$ and $0.41\,\mathrm{nm}^{-1}$, over 200 STM frames (~1 h). No apparent correlations in $G_{ll}(q)$, or $G_{tt}(q)$, for different q values were observed. The average values of G_{ll} are $3\,\mathrm{nm}^4$ and $0.7\,\mathrm{nm}^4$ (with larger uncertainty in the latter), for $q \approx 0.14\,\mathrm{nm}^{-1}$ and $0.41\,\mathrm{nm}^{-1}$, respectively.

The complete phase diagram for this model has been analysed[12], providing some context in which to interpret our results. In particular, the model predicts the existence of a critical fraction, $f_c \approx 0.29$, of the surface covered with islands, such that, for $f \lesssim f_c$, the lowest-energy structure is a triangular lattice of near-circular vacancy islands of narrowly distributed radius, R, and repeat distance, b (but other lattice symmetries can be imposed by the substrate[10]). These predictions are in qualitative agreement with our observations in Fig. 1. There is some disagreement on the predicted versus observed values of R and b, and their dependence on f, but this is not surprising for a model which overlooks details of the reaction with sulphur, the subsequent displacement of Ag atoms, or the potential role of the dislocation network in the Ag film. For higher f, other ordered structures are predicted to form[11,12], but to test the formation of such structures, and related details of the phase diagram, tailored experimental studies are required (K.P. *et al.*, manuscript in preparation).

To estimate the value of γ_d, we used a connection to the elastic constants, λ and μ. If the energy increase due to an isotropic expansion of the lattice unit cell (at constant f) is stored as elastic energy, then one finds $\gamma_d = 3^{1/2}(\lambda + \mu)b^2/(\pi R)$ (K.P. *et al.*, manuscript in preparation). For our estimates of λ and μ, this relation gives $\gamma_d \approx 0.15$–$0.3\,\mathrm{eV\,Å}^{-1}$, using the measured $b \approx 53$ Å and $R \approx 12$ Å. To assess the feasibility of the elastic forces as the root of stable self-organized behaviour, it is also useful to relate γ_d directly to the stress field around the islands. Continuum elasticity considerations[13] obtain $\gamma_d \approx (1 - \nu)\sigma^2/(2\pi\epsilon)$, where ν and ϵ are the Poisson ratio and bulk modulus of the substrate, respectively, and σ is the difference in the surface stress between Ag and Ru regions. Assuming $\nu_{Ru} \approx 0.5$ and $\epsilon_{Ru} \approx 10^{10}\,\mathrm{N\,m}^{-2}$, the estimate of γ_d above implies $\sigma \approx 0.3$–$0.5\,\mathrm{eV\,Å}^{-2}$. This is within the range of σ values reported for unreconstructed metal(111) surfaces[13], providing confidence in our central estimate of γ_d.

The S/Ag/Ru(0001) lattice of vacancy islands is unlikely to be unique: small changes in the type of adsorbate or host film will probably produce new lattices with different parameters (R, b, λ, μ and so on). A possible application of vacancy island lattices is their use as templates for pre-patterning new nanostructures[10], thus allowing properties which are unique to these length scales to be controlled. This relies on the detailed characterization, as reported here, of the forces responsible for the existence of such templates. □

Received 1 June; accepted 5 October 1998.

1. Seul, M. & Andelman, D. Domain shapes and patterns: the phenomenology of modulated phases. *Science* **267,** 476–483 (1995).
2. Itano, W. M. *et al.* Bragg diffraction from crystallized ion plasmas. *Science* **279,** 686–689 (1998).
3. Evans, J. H. Observations of a regular void array in high purity molybdenum irradiated with 2 MeV nitrogen ions. *Nature* **229,** 403–404 (1971).
4. Asai, M., Ueba, H. & Tatsuyama, C. Heteroepitaxial growth of Ge films on the Si(100)-2×1 surface. *J. Appl. Phys.* **58,** 2577–2583 (1985).
5. Kern, K. *et al.* Long-range spatial self-organization in the adsorbate-induced restructuring of surfaces: Cu{110}-(2×1)O. *Phys. Rev. Lett.* **67,** 855–858 (1991).
6. Hörnis, H., West, J. R., Conrad, E. H. & Ellialtioglu, R. Island ordering on clean Pd(110). *Phys. Rev. B* **47,** 13055–13058 (1993).
7. Zeppenfeld, P., Krzyzowski, M. A., Romainczyk, Ch., David, R. & Comsa, G. Stability of disk and stripe patterns of nanostructures at surfaces. *Surf. Sci.* **342,** L1131–L1136 (1995).
8. Haasen, P. *Physical Metallurgy* 256 (Cambridge Univ. Press, New York, 1996).
9. Tersoff, J., Teichert, C. & Lagally, M. G. Self-organization in growth of quantum dot superlattices. *Phys. Rev. Lett.* **76,** 1675–1678 (1996).
10. Parker, T. M., Wilson, L. K., Condon, N. G. & Leibsle, F. M. Epitaxy controlled by self-assembled nanometer-scale structures. *Phys. Rev. B* **56,** 6458–6461 (1997).
11. Vanderbilt, D. Phase segregation and work-function variations on metal surfaces: spontaneous formation of periodic domain structures. *Surf. Sci.* **268,** L300–L304 (1992).
12. Ng, K.-O. & Vanderbilt, D. Stability of periodic domain structures in a two-dimensional dipolar model. *Phys. Rev. B* **52,** 2177–2183 (1995).
13. Ibach, H. The role of surface stress in reconstruction, epitaxial growth and stabilization of mesoscopic structures. *Surf. Sci. Rep.* **29,** 193–263 (1997).

14. Stevens, J. L. & Hwang, R. Q. Strain stabilized alloying of immiscible metals in thin films. *Phys. Rev. Lett.* **74,** 2078–2081 (1995).
15. Hwang, R. Q., Hamilton, J. C., Stevens, J. L. & Foiles, S. M. Near-surface buckling in strained metal overlayer systems. *Phys. Rev. Lett.* **75,** 4242–4245 (1995).
16. Morgenstern, K., Rosenfeld, G., Poelsema, B. & Comsa, G. Brownian motion of vacancy islands on Ag(111). *Phys. Rev. Lett.* **74,** 2058–2061 (1995).
17. de la Figuera, J., Prieto, J. E., Ocal, C. & Miranda, R. Creation and motion of vacancy islands on solid surfaces: a direct view. *Solid State Commun.* **89,** 815–818 (1994).
18. Nelson, D. R. & Halperin, B. I. Dislocation-mediated melting in two dimensions. *Phys. Rev. B* **19,** 2457–2484 (1979).
19. Huse, D. A. Shape of diffraction peaks of a two-dimensional solid. *Phys. Rev. B* **28,** 6110–6111 (1983).
20. Morgenstern, K., Rosenfeld, G. & Comsa, G. Decay of two-dimensional Ag islands on Ag(111). *Phys. Rev. Lett.* **76,** 2113–2116 (1996).

Acknowledgements. This work was supported by the Office of Basic Energy Sciences of the US DOE, Divisions of Materials Science and Chemical Science. J.d.l.F. also acknowledges support from the Fulbright Commission and the Spanish MEC.

Correspondence and requests for materials should be addressed to R.Q.H. (e-mail: rqhwang@california.sandia.gov).

Coordinated proton tunnelling in a cyclic network of four hydrogen bonds in the solid state

Dermot F. Brougham*, Roberto Caciuffo† & Anthony J. Horsewill*

** School of Physics and Astronomy, University of Nottingham, Nottingham NG7 2RD, UK*
† Istituto Nazionale per la Fisica della Materia, Università di Ancona, Dipartimento di Scienze dei Materiali e della Terra, Via Brecce Bianche, I-60131 Ancona, Italy

The transfer of protons involved in hydrogen bonding is fundamental to many chemical and biological processes. Quantum tunnelling can play an important role in this process[1,2]. It manifests itself in strong isotope effects[3,4] and has been observed directly in the solid state[5]. The tunnelling behaviour seen in such studies usually displays the characteristics of a particle confined in a double-well potential. But proton tunnelling can also occur in a coordinated fashion that involves many hydrogen bonds simultaneously. Such a process may significantly affect the properties of linear and circular networks of hydrogen bonds, which occur in ice and in macromolecules containing hydroxyl groups[6,7]. Here we report the direct observation by NMR relaxometry of coordinated proton tunnelling in a cyclic array of four hydrogen bonds in solid *p*-tert-butyl calix[4]arene at low temperature. We are able to quantify the parameters that describe this phenomenon and find good agreement with theoretical predictions for phonon-assisted tunnelling[8].

Calix[*n*]arenes are bowl-shaped synthetic macrocycles with ordered arrays of hydrogen-bonded phenol-methylene oligomers[9]. The number of the phenolic units can vary from $n = 3$ to $n = 14$, and different substituents can be attached to the aromatic ring in the *para* position and at the phenolic oxygen. The *p*-tert-butyl calix[4]arene molecule possesses four-fold symmetry and assumes a shape (shown in Fig. 1a) that is maintained by a cyclic array of four hydrogen bonds[10].

NMR relaxometry is a well-established experimental technique for the study of molecular dynamics. The molecular motion modulates the nuclear magnetic interactions in which the nucleus participates, and hence drives the transitions that mediate the establishment of equilibrium amongst the nuclear spin energy levels. Therefore, information on the rates and frequencies that characterize the molecular motion is encoded within the nuclear spin relaxation properties.

In the system studied here, the modulation of the nuclear dipole–dipole interactions dominates the proton spin relaxation. In the case where the dynamics are stochastic, the time correlation function for the proton position is an exponential decay, and its Fourier transform, which determines the spin–lattice relaxation rate $T_1^{-1}(\omega)$, has lorentzian form in the frequency domain. As single-spin and double-spin flip transitions are possible, T_1^{-1} samples the motional spectrum at one and two times the proton Larmor frequency, ω_L. Measurements of T_1^{-1} as a function of an external magnetic field, B, will therefore give a direct measurement of the spectral density function because $\omega = \gamma B$ (where the magnetogyric ratio $\gamma = 2.675 \times 10^8\ s^{-1}\ T^{-1}$). In the case where the molecular system interchanges between two tautomeric configurations, labelled a and b, then for a powdered material[11]

$$T_1^{-1}(\omega_L) = C p_a p_b \left[\frac{\tau_c}{1 + \omega_L^2 \tau_c^2} + \frac{4\tau_c}{1 + (2\omega_L)^2 \tau_c^2} \right] \qquad (1)$$

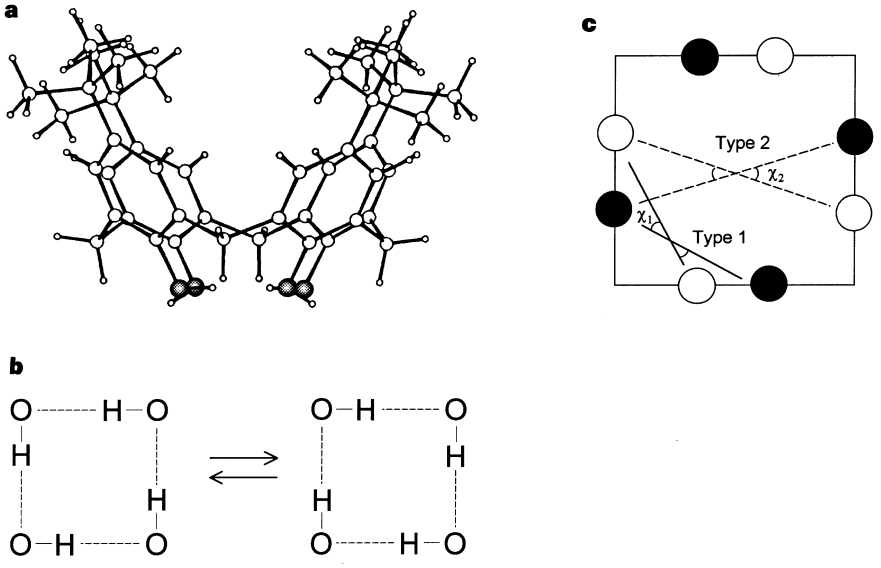

Figure 1 Coordinated proton tunnelling in *p*-tert-butyl calix[4]arene. A side view of the molecular conformation of this compound, perpendicular to the four-fold symmetry axis, is shown in **a**. The oxygen atoms participating in the cyclic hydrogen bond array are shaded. The interconversion between the two tautomers schematically shown in **b** can be achieved by coordinated proton tunnelling. The relevant geometrical parameters for determining the motion-induced changes in the proton dipolar interactions are defined in **c**, where the hydrogen atoms are indicated by open circles for tautomer a, and filled circles for tautomer b.